

# Rich 1T-MoS<sub>2</sub> Nanoflowers Decorated on Reduced Graphene Oxide Nanosheet for Ultra-Quick Zn<sup>2+</sup> Storage

Fei Long,<sup>[a, b]</sup> Junjie Shi,<sup>[b]</sup> Qixiang Zhang,<sup>[b]</sup> Zunyu Liu,<sup>[b]</sup> Yixin Hou,<sup>[b]</sup> Ke Mao,<sup>[a, b]</sup> Nishuang Liu,<sup>[b]</sup> Luying Li,<sup>[b]</sup> Fei Long,<sup>\*[a]</sup> and Yihua Gao<sup>\*[a, b]</sup>

Aqueous zinc-ion batteries (AZIBs) with low cost and high safety are promising energy storage equipment for large-scale grids. However, the further development of AZIBs is obstructed by finite usability of cathode materials. Recently, layered materials represented by MoS<sub>2</sub> have attracted attentions because they can provide facile two-dimensional (2D) channels for the diffusion of Zn<sup>2+</sup>, but low capacity and poor rate capability limit their applications. Herein, two classical layered materials are combined to form a stable heterostructure (MoS<sub>2</sub>-rGO) by in-situ growing metallic 1T-MoS<sub>2</sub> nanoflowers on reduced graphene oxide (rGO) to provide more 2D channels for electrons

transfer and Zn<sup>2+</sup> diffusion. The MoS<sub>2</sub>-rGO heterostructure exhibits high specific capacity (303.10 mAh g<sup>-1</sup> at 0.20 A g<sup>-1</sup>) and ultrahigh rate capability (102.70 mAh g<sup>-1</sup> at 20.00 A g<sup>-1</sup>, i.e., capacity retention of 33.88% for a 100-fold increase in current density) in aqueous electrolyte. Furthermore, the quasi-solid-state aqueous zinc-ion battery based on MoS<sub>2</sub>-rGO heterostructure also shows high electrochemical performance at bending states and extreme temperature. This work provides an inspiration for construction of AZIBs with high-performance layered cathode.

## Introduction

Electrochemical energy storage (EES) devices are a predominant support for large-scale grids.<sup>[1–3]</sup> Among various battery systems, lithium-ion batteries (LIBs) quickly occupied the main power market owing to their high energy density. However, the applications of LIBs in large-scale grids are limited due to their high price caused by the shortage of lithium resources and the flammability of organic electrolytes.<sup>[4–10]</sup> Recently, aqueous zinc-ion batteries (AZIBs) have been considered as a hopeful alternative to LIBs due to their fascinating properties, including the relatively low redox potential (−0.763 V vs. standard hydrogen electrode), high theoretical specific capacity (820 mAh g<sup>-1</sup> and 5851 mAh cm<sup>-3</sup>), non-toxicity and low cost thanks to the use of zinc metal anodes. In addition, the adoption of aqueous electrolytes is safe and environmentally friendly.<sup>[11–17]</sup> However, the slow intercalation behavior of Zn<sup>2+</sup>

makes it a substantial challenge to explore suitable cathode materials.<sup>[18–21]</sup>

Until now, many types of layered materials have been developed for the cathode of AZIBs, such as manganese-based (e.g., MnO<sub>2</sub> and ZnMn<sub>2</sub>O<sub>4</sub>),<sup>[22,23]</sup> vanadium-based ones (e.g., V<sub>2</sub>O<sub>5</sub>·nH<sub>2</sub>O and Zn<sub>3</sub>V<sub>2</sub>O<sub>7</sub>(OH)<sub>2</sub>·2H<sub>2</sub>O),<sup>[24,25]</sup> Prussian blue analogues (PBAs, e.g., Na<sub>2</sub>MnFe(CN)<sub>6</sub> and K<sub>2</sub>MnFe(CN)<sub>6</sub>),<sup>[26,27]</sup> and others. In particular, layered transition-metal disulfides represented by MoS<sub>2</sub>, have been considered as potential cathode materials for AZIBs because their unique layered structure provides more moderate 2D diffusion channels and effectively improves the transport of zinc ions.<sup>[28–31]</sup> However, the reversible insertion and extraction of hydrated zinc ions needs to overcome the higher energy barrier due to the limitation of the strong electrostatic interaction between neighboring MoS<sub>2</sub> layers with a narrow interlayer spacing (0.62 nm).<sup>[32–34]</sup> To extenuate these problems, reasonable design strategies have been proposed to improve the electrochemical performance of MoS<sub>2</sub> cathode.

Zhi and co-workers reported that the glucose-assisted hydrothermal method synthesized 0.70 nm spacing MoS<sub>2</sub> nanosheets cathode on carbon cloth, which showed good specific capacities of 199.30 mAh g<sup>-1</sup> at 0.10 A g<sup>-1</sup> and 101.80 mAh g<sup>-1</sup> at 4.00 A g<sup>-1</sup>.<sup>[35]</sup> In another work, Wang and co-workers inserted crystal water into the MoS<sub>2</sub> layers through a simple hydrothermal method, which expanded the interlayer distance to 0.68 nm and improved the surface hydrophilicity, which showed the specific capacity of 182.00 mAh g<sup>-1</sup> at 0.10 A g<sup>-1</sup> and 92.00 mAh g<sup>-1</sup> at 4.00 A g<sup>-1</sup>.<sup>[36]</sup> Soon afterwards, Li and co-workers reported that the MoS<sub>2</sub> interlayer spacing was expanded to 0.96 nm by means of manufacturing structural defects and doping O atoms, which improved the hydrophilicity and conductivity of MoS<sub>2</sub>. As a result, the prepared cathode exhibited the high specific capacity (261.00 mAh g<sup>-1</sup> at

- [a] F. Long, K. Mao, Prof. F. Long, Prof. Y. Gao  
School of Materials Science and Engineering  
Guangxi Key Laboratory of Optical and Electronic Materials and Devices &  
Collaborative Innovation Center for Exploration of Nonferrous Metal De-  
posits and Efficient Utilization of Resources  
Guilin University of Technology (GUT)  
541004 Guilin, China  
E-mail: longf@glut.edu.cn  
gaoyihua@hust.edu.cn
- [b] F. Long, J. Shi, Q. Zhang, Z. Liu, Y. Hou, K. Mao, Dr. N. Liu, Prof. L. Li,  
Prof. Y. Gao  
Center for Nanoscale Characterization & Devices (CNCD)  
School of Physics & Wuhan National Laboratory for Optoelectronics (WNLO)  
Huazhong University of Science and Technology (HUST)  
430074 Wuhan, China
-  Supporting information for this article is available on the WWW under  
<https://doi.org/10.1002/batt.202200110>

0.10  $\text{A g}^{-1}$ ) and an excellent rate capability (102.40  $\text{mAh g}^{-1}$  at 10.00  $\text{A g}^{-1}$ ).<sup>[37]</sup> As mentioned above, a series of encouraging advancements have been reported in recent years and the specific capacity of  $\text{MoS}_2$  has been indeed improved considerably thanks to many mainstream strategies for expanding the interlayer spacing. However, few other effective strategies have been developed expanding the  $\text{MoS}_2$  interlayer distance, the specific capacity and rate capability of  $\text{MoS}_2$  are still not satisfactory. Therefore, it is still an interesting challenge to develop the  $\text{MoS}_2$  cathode that can quickly store  $\text{Zn}^{2+}$  to achieve higher specific capacity and excellent rate capability. Generally,  $\text{MoS}_2$  has two different phases: metallic 1T-phase and semiconducting 2H-phase.<sup>[38]</sup> The 1T- $\text{MoS}_2$  has more amusing features, such as unique metallic electronic structure and lower  $\text{Zn}^{2+}$  diffusion barrier, which makes it more active.<sup>[39,40]</sup> Therefore, the high content of 1T- $\text{MoS}_2$  is expected to improve the electrochemical performance of the  $\text{MoS}_2$  cathode. Besides, reduced graphene oxide (rGO) with excellent electrical conductivity has been confirmed as a perfect material in EES devices.<sup>[41–44]</sup> Consequently, it is feasible to design a cathode with high specific capacity and excellent rate performance by decorating rich metallic 1T- $\text{MoS}_2$  nanoflowers on rGO nanosheets.

In this work, a novel strategy to microscopically promote the storage of  $\text{Zn}^{2+}$  in  $\text{MoS}_2$  was proposed, which is different from the mainstream strategies (expand the interlayer spacing of  $\text{MoS}_2$ ). Some  $\text{MoS}_2$  nanoflowers were uniformly in-situ grown on rGO nanosheet to prepare  $\text{MoS}_2$ -rGO heterostructure. The prepared  $\text{MoS}_2$  nanoflowers are very small, which provides a lot of easy-to-contact reaction areas for the adsorption and diffusion of  $\text{Zn}^{2+}$  on the electrode. Meanwhile, the highly efficient synergistic effect of the abundant metallic 1T-phase and the highly conductive rGO effectively boosts the transfer of electrons and the reversible insertion/extraction of  $\text{Zn}^{2+}$ . Because of these improvements, the  $\text{MoS}_2$ -rGO cathode demonstrates high specific capacity, excellent rate capability (303.10  $\text{mAh g}^{-1}$  at 0.20  $\text{A g}^{-1}$  with 102.70  $\text{mAh g}^{-1}$  at 20.00  $\text{A g}^{-1}$ , 33.88% capacity retention after the current density was increased 100-fold) and stable cycle performance (65.70% capacity retention after 1000 charge-discharge cycles). Moreover, the electrode reaction kinetics involving pseudo-capacitance behavior and transfer energy barrier were studied by cyclic voltammetry (CV), galvanostatic charge-discharge (GCD) and density functional theory (DFT). Furthermore, the mechanism of zinc-ion storage in  $\text{MoS}_2$ -rGO during charge and discharge was revealed by ex-situ laser confocal Raman spectroscopy and X-ray photoelectron spectroscopy (XPS). Finally, the quasi-solid-state aqueous  $\text{Zn}/\text{MoS}_2$ -rGO battery developed by polyacrylamide-polyethylene glycol/zinc trifluoromethanesulfonic acid (PAM-PEG/ $\text{Zn}(\text{CF}_3\text{SO}_3)_2$ ) hydrogel electrolyte shows high electrochemical performance at bending states and extreme temperature. This work provides an inspiration for the study of high-performance layered cathode materials for AZIBs.

## Results and Discussion

As shown in Figure 1(a), the  $\text{MoS}_2$ -rGO was readily acquired by one-pot solvothermal reaction. In this reaction, GO is reduced to rGO in the presence of a strong reducing agent hydrazine hydrate in N, N-dimethylformamide (DMF) as a solvent, which controls the nucleation and growth of  $\text{MoS}_2$  nanoflowers in the subsequent reaction. Meanwhile, ammonium tetrathiomolybdate and urea react together and grow into  $\text{MoS}_2$  nanoflowers uniformly on the surface of rGO. The transmission of electrons and zinc ions diffusion during the charge and discharge process based on  $\text{MoS}_2$ -rGO cathode of AZIBs is also showed in Figure 1(b). During discharge, the  $\text{Zn}^{2+}$  anions in  $\text{Zn}(\text{CF}_3\text{SO}_3)_2$  electrolyte move toward the  $\text{MoS}_2$ -rGO cathode. Meanwhile, zinc ions are adsorbed and embedded to the cathode. At this time, rGO will collect as much electrons from the external circuit as possible and quickly import it to the electrode to complete discharge. During charge, the zinc ions are returned from the  $\text{MoS}_2$ -rGO cathode to the  $\text{Zn}(\text{CF}_3\text{SO}_3)_2$  electrolyte and moved to the Zn anode. Meanwhile, zinc ions are separated from the cathode and transferred to the anode through electrolyte to form zinc. Currently, rGO quickly export the electrons through the external circuit to complete the charge. Through elaborate conception and reasonable design, we expect that  $\text{MoS}_2$ -rGO can quickly store zinc ions and conduct electrons when used as AZIBs cathode, so that the assembled battery has relatively high specific capacity, excellent rate capability and relatively long cycle life.

The successful synthesis of  $\text{MoS}_2$ -rGO and pristine  $\text{MoS}_2$  were demonstrated by a series of characterizations. The XRD patterns of  $\text{MoS}_2$ -rGO and pristine  $\text{MoS}_2$  in Figure 2(a) accurately detected (002) characteristic peaks of the highly conductive metallic 1T-phase at  $2\theta = 9.20^\circ$  and  $9.10^\circ$ , respectively, indicating that the prepared materials are rich in 1T-phase. The (002) characteristic peak of  $\text{MoS}_2$ -rGO is much stronger than pristine  $\text{MoS}_2$ , suggesting that rGO is an ideal growth platform for 1T- $\text{MoS}_2$ . In addition, the characteristic peak of (100) of the semiconductor 2H-phase was detected in the XRD patterns, manifesting that the prepared materials are a coexistence state of 1T-phase and 2H-phase. Finally, the XRD pattern of  $\text{MoS}_2$ -rGO also showed a characteristic peak at  $2\theta = 24.5^\circ$ , which is consistent with the (002) characteristic peak of rGO at  $2\theta = 23.6^\circ$  (Figure S1a). The Raman spectra (Figure 2b) of  $\text{MoS}_2$ -rGO and pristine  $\text{MoS}_2$  both accurately showed the characteristic peaks ( $J_2$ ) and ( $J_3$ ) of the 1T-phase, which are attributed to the phonon modes in 1T- $\text{MoS}_2$  superlattice structure.<sup>[45,46]</sup> Moreover, the intensity ratio of the D band (defect vibration) to the G band (graphitic carbon vibration) of  $\text{MoS}_2$ -rGO is as high as 1.33, demonstrating the formation of abundant rGO with rich defects (Figures 2b and S1b). Importantly, these defects on rGO can provide lots of excellent adsorption and intercalation sites for zinc ions, so that zinc ions can be stored more and faster.<sup>[47]</sup> The characteristic peak of Mo-S dangling bonds ( $g=2.003$ ) in the electron paramagnetic resonance (EPR) spectrum indicated the existence of S vacancies (Fig-

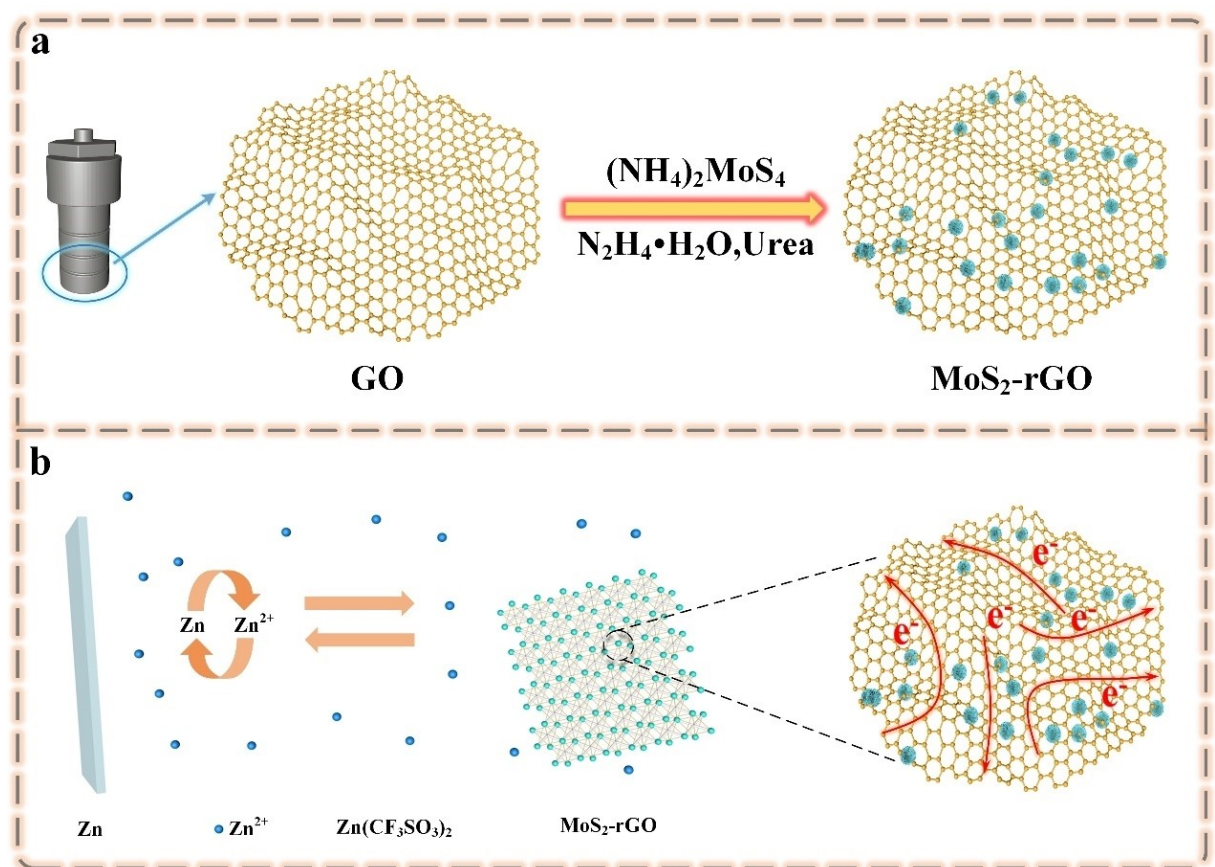
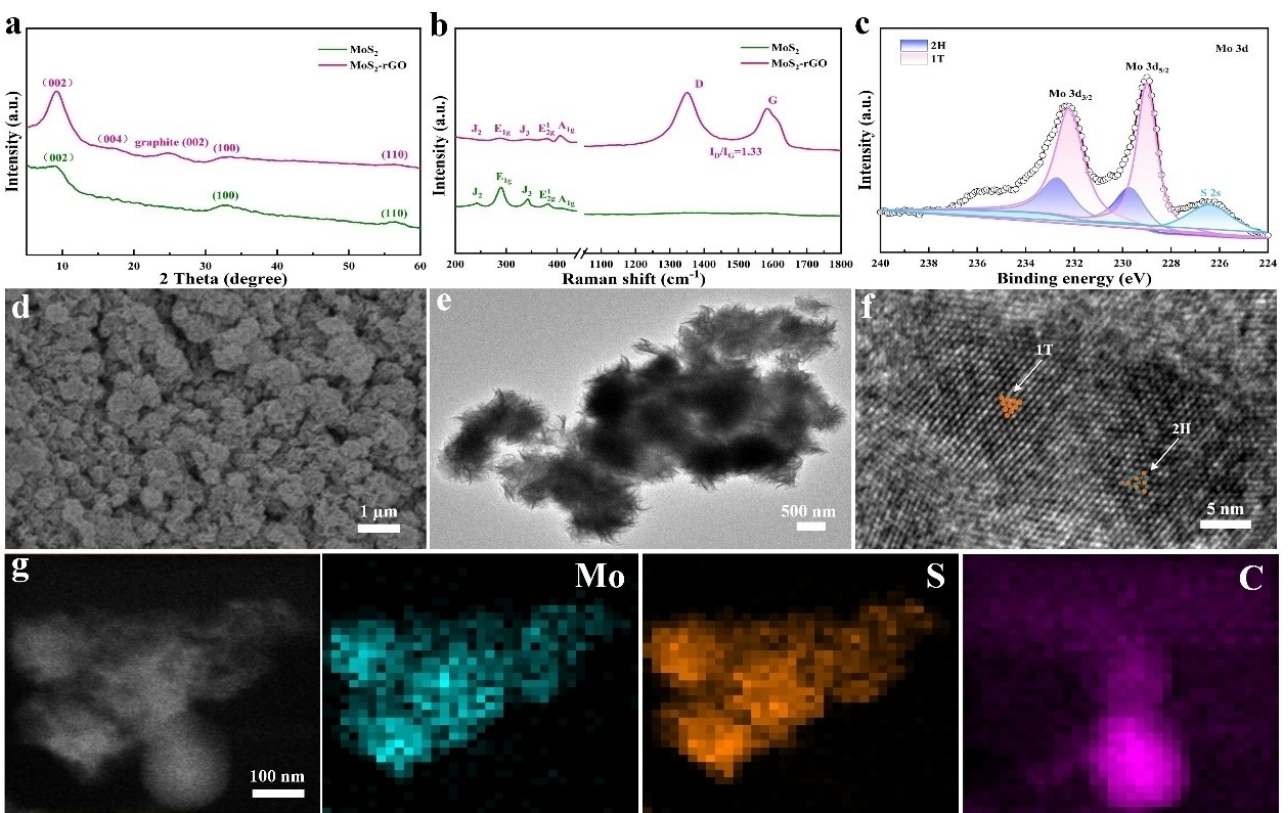


Figure 1. Schematic illustration. a) Synthesis process. b) Energy storage mechanism.

ure S2), significantly, these sulfur vacancies in MoS<sub>2</sub> offer numerous locations that are almighty conducive to the chemisorption and storage of zinc ions.<sup>[48,49]</sup> X-ray photoelectron spectroscopy (XPS) analysis was performed (Figures 2c and S3) to illustrate the surface chemical composition and electronic states of the samples. The XPS pattern (Figure S3d) of MoS<sub>2</sub>-rGO clearly exhibited distinct peaks at 162.3, 229.1, 284.8, 396.7, and 531.9 eV, corresponding to S 2p, Mo 3d, C 1s, N 1s, and O 1s, respectively. There were two doublet bands that correspond to the Mo<sup>4+</sup> 3d<sub>5/2</sub> and Mo<sup>4+</sup> 3d<sub>3/2</sub> electrons, respectively (Figure 2c). The lower binding energy peaks at 229.0 and 232.3 eV correspond to abundant 1T-phase, while the higher binding energy peaks at 229.8 and 232.7 eV correspond to a few 2H-phase. The ratio of 1T-MoS<sub>2</sub>:2H-MoS<sub>2</sub> in MoS<sub>2</sub>-rGO heterostructure was calculated to be about 2.50:1.00 from the peak area. In the high-resolution XPS spectrum of Mo 3d (Figure S3b), the main characteristic peaks centered around 229.0 and 232.3 eV were measured. Corresponding to Mo<sup>4+</sup>, the peaks appearing at 230.4, 233.3, 232.9 and 235.6 eV are related with Mo<sup>5+</sup> and Mo<sup>6+</sup>. The Mo<sup>6+</sup> may be the result of surface oxidation of MoS<sub>2</sub>, while Mo<sup>5+</sup> is reduced from Mo<sup>6+</sup>.<sup>[50,51]</sup> In the high-resolution XPS spectrum of S 2p (Figure S3c), the peaks located at 162.0 and 163.2 eV are assigned to apical S<sup>2-</sup> species and bridging S<sub>2</sub><sup>2-</sup>, respectively. The high-resolution XPS spectrum peaks of C 1s (Figure S3a) were

measured at 284.8 and 285.5 eV positions, which are consistent with C-C and C=C, respectively. The perfect combination of rich metallic 1T-MoS<sub>2</sub> and highly conductive rGO was demonstrated by these results. Therefore, MoS<sub>2</sub>-rGO will promote the redox reaction and accelerate the transport of electrons. Thermogravimetric analysis-differential thermal analysis (TGA-DTA) curves (Figure S4) confirmed the absence of structural water in MoS<sub>2</sub>-rGO. Scanning electron microscopy (SEM, Figure 2d) image clearly revealed the microscopic morphology of the MoS<sub>2</sub> nanoflowers, which are minute in size (about 100 nm) and uniformly distributed. Transmission electron microscopy images (TEM, Figures 2e and S5) clearly illustrated the inseparable contact between MoS<sub>2</sub> nanoflowers and 2D graphene nanosheets, which is highly beneficial for rapid interfacial charge transfer. MoS<sub>2</sub> nanoflowers were evenly distributed on the surface of rGO without agglomeration, evincing rGO is a perfect 2D template for inducing the homogeneous nucleation and growth of MoS<sub>2</sub>. Meanwhile, the HRTEM image clearly showed the abundant 1T-phase triangular lattices along with some 2H-phase honeycomb lattices in MoS<sub>2</sub>-rGO (Figure 2f).<sup>[45,50]</sup> The high-angle annular dark field scanning TEM (HAADF-STEM, Figure 2g) image further confirmed the 2D nanoflowers of MoS<sub>2</sub>-rGO, and the corresponding elemental mapping image displayed the homogeneous distribution of Mo and S in MoS<sub>2</sub>-rGO, verifying that MoS<sub>2</sub> nanoflowers



**Figure 2.** Characterizations. a) XRD pattern and b) Raman spectra of  $\text{MoS}_2$ -rGO and pristine  $\text{MoS}_2$ . c) XPS pattern of Mo 3d in  $\text{MoS}_2$ -rGO. d) SEM, e) TEM, f) HRTEM and g) HAADF-STEM elemental mapping images of  $\text{MoS}_2$ -rGO.

nucleate and grow uniformly throughout the entire graphene surface. Flower-like  $\text{MoS}_2$  nanosheets uniformly distributed on rGO provide more active sites for the reaction between electrodes, simultaneously, the tightly connected heterogeneous interface between  $\text{MoS}_2$  nanoflowers and rGO not only ensures the high structural stability of  $\text{MoS}_2$ -rGO, but also provides more 2D diffusion channels for the diffusion of zinc ions. Therefore, the  $\text{MoS}_2$ -rGO cathode is expected to accelerate the electron transfer and storage of zinc ions, leading to higher capacity and better rate capability for batteries.

The electrochemical performance of the different  $\text{MoS}_2$ -rGO cathodes developed by adjusting the weight of GO were tested using a two-electrode system (metal zinc foil anode,  $\text{MoS}_2$ -rGO cathode and 2 M  $\text{Zn}(\text{CF}_3\text{SO}_3)_2$  electrolyte). There was no significant difference in the specific capacity of active materials with different loads (Figure S6). As shown in Figure 3(a), the cyclic voltammetry (CV) curves of the different  $\text{MoS}_2$ -rGO cathodes developed by adjusting the weight of GO at the sweep rate of  $1.00 \text{ mV s}^{-1}$  had the similar shape and different peak current densities. Remarkably, the CV curve of  $\text{MoS}_2$ -rGO cathode with 10 GO showed a pair of obvious redox peaks at  $0.31/1.42 \text{ V}$  vs.  $\text{Zn}^{2+}/\text{Zn}$ , corresponding to the  $\text{Zn}^{2+}$  insertion/extraction behaviors. However, the redox peaks of  $\text{MoS}_2$ -rGO cathode with 5GO or 20 GO were relatively faint, implying typical surface adsorption/desorption capacitance behavior. Electrochemical impedance spec-

troscopy (EIS, Figure S7) further indicated that  $\text{MoS}_2$ -rGO cathode with 10 GO has the lowest charge transfer resistance ( $R_{ct}$ ) among  $\text{MoS}_2$ -rGO with different GO contents. The reason may be that the addition of too little or too much GO will lead to poor nucleation of  $\text{MoS}_2$  and layer stacking of  $\text{MoS}_2$  and rGO, which is detrimental to the transmission of electrons and the storage of  $\text{Zn}^{2+}$ . GCD curves of the cathode with various GO additions were illustrated in Figures 3(c) and S8. The relationship between the specific capacity and current density of cathodes with different GO additions were calculated from the GCD results (Figure 3b). In contrast, the specific capacity of the  $\text{MoS}_2$ -rGO cathode with 10 GO addition was the highest among different GO addition cathodes, furthermore, an ultrahigh rate capability ( $102.70 \text{ mAh g}^{-1}$  at  $20.00 \text{ A g}^{-1}$ , i.e., capacity retention of 33.88% for a 100-fold increase in current density) and a high specific capacity ( $303.10 \text{ mAh g}^{-1}$  at  $0.20 \text{ A g}^{-1}$ ) were achieved by the  $\text{MoS}_2$ -rGO cathode with 10 GO addition. The breathtaking thing is that, as far as we know, the  $\text{MoS}_2$ -rGO cathode with 10 GO addition has the best specific capacity and rate capability among  $\text{MoS}_2$  cathode materials that have been reported for AZIBs (Table S1). Therefore, the  $\text{MoS}_2$ -rGO cathode with 10 GO addition was chosen for the next in-depth study. As shown in Figure 3(c), the specific capacities of the specific capacities of  $\text{MoS}_2$ -rGO cathode with 10 GO addition are  $303.10$ ,  $284.20$ ,  $260.40$ ,  $238.60$ ,  $212.20$ ,  $200.50$ ,  $173.70$ ,  $136.80$ , and  $102.70 \text{ mAh g}^{-1}$  at  $0.20$ ,  $0.50$ ,  $1.00$ ,  $2.00$ ,

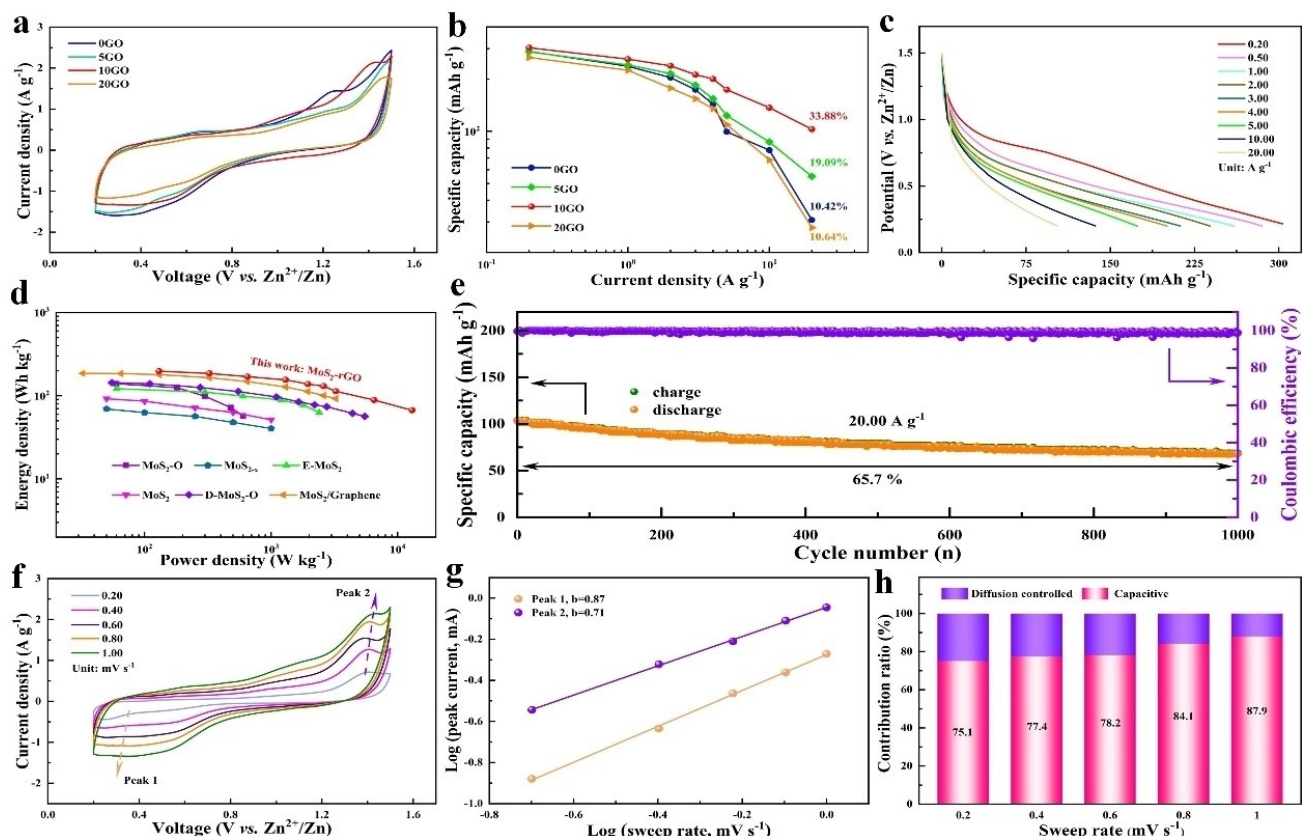


**Figure 3.** Electrochemical performances and electrode process kinetics of MoS<sub>2</sub>-rGO. MoS<sub>2</sub>-rGO with different GO additions, a) CV curves at 1.00 mVs<sup>-1</sup> and b) specific capacities at different current densities. c) Discharge curves at various current densities of optimal MoS<sub>2</sub>-rGO cathode. d) Energy and power densities. e) Cycle life at 20.00 Ag<sup>-1</sup>. f) CV curves at increasing sweep rates from 0.20 to 1.00 mVs<sup>-1</sup>. g) The corresponding log(*i*) versus log(*v*) plots at peak 1 and peak 2. h) Capacitive-limited and diffusion-controlled contributions to capacity at different sweep rates from 0.20 to 1.00 mVs<sup>-1</sup>.

3.00, 4.00, 5.00, 10.00, and 20.00 A g<sup>-1</sup>, respectively. As notably highlighted in Figure 3(d), the present MoS<sub>2</sub>-rGO cathode manifests higher energy densities over a wider power densities range compared to the recently reported MoS<sub>2</sub> cathodes for AZIBs, which has the power density and energy density as high as 13000.00 W kg<sup>-1</sup> and 197.10 Wh kg<sup>-1</sup>, respectively. The cycle life was tested under a high current density of 20.00 A g<sup>-1</sup> to further illustrate the excellent performance of MoS<sub>2</sub>-rGO cathode with 10 GO addition. As a result, the capacity retention of MoS<sub>2</sub>-rGO cathode with 10 GO remained 65.70% after 1000 charge-discharge cycles (Figure 3e). A few nanoflowers disintegrated after 1000 cycles at a large current, resulting in interlayer stacking, which may lead to capacity decay (Figure S9a). The XRD peak positions remained highly consistent before and after cycling, indicating the electrode material has not changed (Figure S9b). Furthermore, 84.60% capacity retention remained after 20 cycles at 0.20 A g<sup>-1</sup> (Figure S10). As shown in Figure 3(f), the electrochemical reaction kinetics of MoS<sub>2</sub>-rGO cathode were revealed by measuring the CV curves at different sweep rates from 0.20 to 1.00 mVs<sup>-1</sup>. The anodic and cathodic peaks move to higher and lower potentials respectively along with the sweep rate increases uniformly, which is caused by the enlarged electrode polar-

ization at high sweep rates. The electrochemical reaction kinetics can be assessed by the following equation:

$$i = av^b \quad (1)$$

Here, *a* and *b* are adjustable parameters, *i* and *v* represent the peak current and the corresponding sweep rate, respectively. Generally, the value range of factor *b* is between 1/2 and 1, specially, *b*=1/2 signifies a diffusion-controlled electrochemical process and *b*=1 indicates a capacitive-limited process. As shown in Figure 3(g), the value of factor *b* can be obtained from the slope of the plot log (*i*)/log (*v*). Evidently, the *b* value of peak 1 (cathodic) and peak 2 (anodic) are 0.87 and 0.71, respectively, revealing that the electrochemical redox reaction is consist of both capacitive and diffusion processes. The capacitive contribution and the diffusion-controlled contribution at a designated sweep rate can be evaluated according to the following equation:<sup>[52]</sup>

$$i(V) = k_1 v + k_2 v^{1/2} \quad (2)$$

where *i*(*V*) is the current at a fixed potential (*V*), and *k*<sub>1</sub>*v* and *k*<sub>2</sub>*v*<sup>1/2</sup> correspond to the capacitive-limited and diffusion-controlled contribution, respectively. As depicted in Figures 3(h) and S11, the contribution ratio of the capacitive process

is 75.10%, 77.40%, 78.20%, 84.10%, and 87.90% at 0.20, 0.40, 0.60, 0.80, and 1.00 mVs<sup>-1</sup>, respectively. Apparently, the capacitive contribution is increasing, which attributes to the fact that diffusion-controlled process is much slower than surface capacitive effect, as a result, the contribution ratio of the capacitive process increases incrementally along with the cumulative sweep rate and the capacitive process plays a leading role in the total capacity.

To disclose the energy storage mechanism of MoS<sub>2</sub>-rGO, ex-situ Raman and XPS spectroscopy tests were performed. As shown in Figure 4(a), the marked states at the initial discharge/charge (points A–E) were selected for the ex-situ Raman spectra tests. The Raman spectra of different discharge/charge depths in the first cycle were exhibited in Figure 4(b). The value of intensity ratio  $I$  ( $A_{1g}/E_{2g}^1$ ) decreased from  $I_A=2.43$  to  $I_C=1.24$  when discharging from 1.50 to 0.20 V, which can be assigned to the change of the Mo valence and the interaction between layers due to the insertion of Zn<sup>2+</sup>. Besides,  $I_C=1.24$  increased to  $I_E=2.35$  when charging from 0.20 to 1.50 V, indicating that Zn<sup>2+</sup> had been extracted from the MoS<sub>2</sub> layers. These results

well demonstrate that the zinc ions storage process is reversible.

The chemical configurations of MoS<sub>2</sub>-rGO at the pristine, fully discharged, and charged states were investigated by ex-situ XPS spectroscopy (Figure 4c and d). The Mo valence in the pristine MoS<sub>2</sub>-rGO is mainly composed of a large amount of Mo<sup>4+</sup> and a small amount of Mo<sup>5+</sup>, Mo<sup>6+</sup>. While in the fully discharged state (0.20 V), most of the low-valence Mo<sup>3+</sup> appears, which means that the insertion of Zn<sup>2+</sup> is accompanied with the decrease of Mo<sup>4+</sup>, simultaneously, the S 2s peak shifts to a lower binding energy owing to the reduction of Mo<sup>4+</sup>. In the process of charging to 1.50 V, the Mo 3d valence and S 2s vibrations recover to their original states, revealing that there is a reversible redox reaction between Mo<sup>5+/4+</sup> and Mo<sup>4+/3+</sup>. As illustrated in Figure 4(d), there is no Zn 2p peaks in the XPS spectra of pristine MoS<sub>2</sub>-rGO. Besides, the MoS<sub>2</sub>-rGO cathode fully discharged to 0.20 V displays strong Zn 2p peaks, and the Zn 2p peaks intensity almost dissipated after charging to 1.50 V, which confirms the successful insertion/extraction of Zn<sup>2+</sup>. This is also the same as the ex-situ

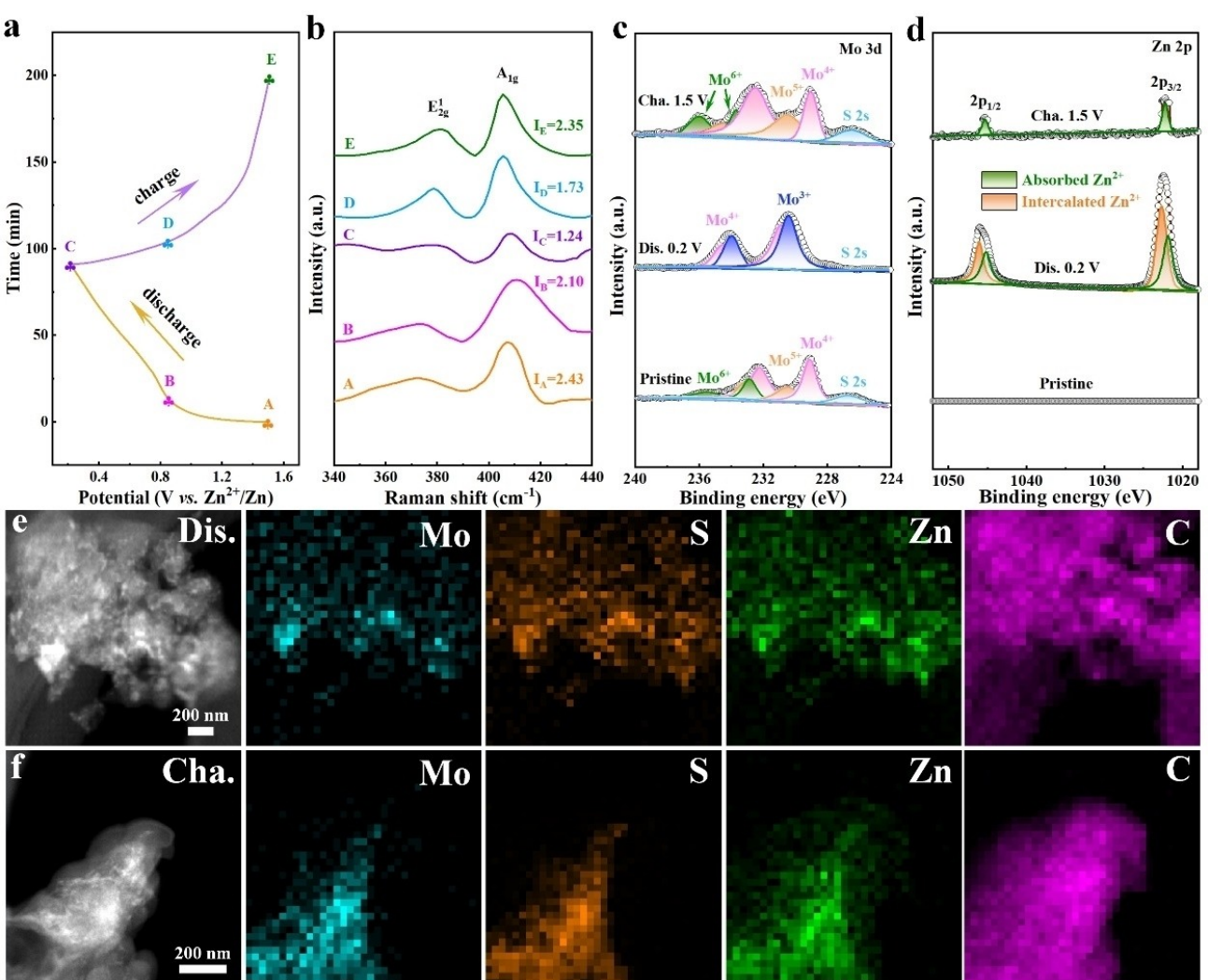


**Figure 4.** Zn-storage mechanism of optimal MoS<sub>2</sub>-rGO. a) Initial GCD curve at 0.20 A g<sup>-1</sup>, the marked states are selected for ex-situ tests. b) Ex-situ Raman spectra, XPS spectra of c) Mo 3d and d) Zn 2p. e, f) HAADF-STEM elemental mapping images of MoS<sub>2</sub>-rGO cathode at the fully discharged and charged states.

Raman spectra analysis, which once again suggests that the insertion/extraction of  $Zn^{2+}$  in the electrode is reversible. At last, a fully charged  $MoS_2$ -rGO cathode only shows one pair of Zn 2p signals, which is attributed to the adsorption of electrolyte on the surface. HAADF-STEM images with corresponding elemental mappings of  $MoS_2$ -rGO cathode at the fully discharged and charged states further illuminates that  $Zn^{2+}$  were magnificently stored in the  $MoS_2$ -rGO cathode (Figure 4e and f). Respectively, Mo, S, and Zn elements are uniformly dispersed (Figure 4e), indicating the successful intercalation of  $Zn^{2+}$ . The Zn element signal can still be detected in Figure 4(f), which is due to the surface adsorption of  $Zn^{2+}$  from the  $Zn(CF_3SO_3)_2$  electrolyte. In short, these observations are consistent with ex-situ Raman and XPS spectra results and visually exhibit the reversible insertion/extraction of  $Zn^{2+}$  in the  $MoS_2$ -rGO material layers.

To further determine the kinetic behavior of  $Zn^{2+}$  migration in  $MoS_2$ -rGO heterostructure, density functional theory (DFT) calculations were performed. The  $Zn^{2+}$  diffusion paths in the models of pristine  $MoS_2$  and  $MoS_2$ -rGO heterostructure are indicated in Figure 5(a-d). Since  $Zn^{2+}$  leaping directly from one octahedral (O) site to the adjacent O site needs high activation energy, so most  $Zn^{2+}$  is usually inserted first in the O center site between  $MoS_2$  layers, where there is enough diffusion space. In the subsequent diffusion process, the  $Zn^{2+}$  will pass through the adjacent metastable tetrahedral (T) site and diffuse from one O site to another O site. In addition, the diffusion of ions must overcome certain migration energy barriers, and high migration energy barriers are extremely unfavorable for the rapid migration of ions. As shown in Figure 5e, the ionic migration energy barriers of  $MoS_2$ -rGO (0.803 eV) are much lower than that of pristine  $MoS_2$  (1.476 eV), revealing that rGO efficiently paved the way for the  $Zn^{2+}$  diffusion between  $MoS_2$  layers. The

partial density (PDOS) and total density of states (DOS) of  $MoS_2$ -rGO are not zero at the Fermi level (Figure 5f), indicating there are plentiful active electrons in the material.<sup>[53]</sup> These active electrons are due to the enhanced conductivity brought by the abundant metallic 1T-phase and the super 2D conductive network of rGO. In a word, the heterostructure effectively ameliorates the layer stacking of  $MoS_2$ , furthermore, the synergistic effect of rGO and high-content 1T-phase enhances the electronic conductivity and successfully boosts the  $Zn^{2+}$  diffusion. Consequently, the capability to ultra-quick store  $Zn^{2+}$  is also noticeably improved.

The admirable electrochemical performance and desirable flexibility of the  $MoS_2$ -rGO cathode promote its application in flexible electronic devices. As shown in Figure 6(a), the flexible quasi-solid-state zinc ion battery ( $MoS_2$ -rGO//Zn battery) is assembled by the flexible galvanized carbon cloth anode (Figure S12),  $MoS_2$ -rGO cathode and PAM-PEG/ $Zn(CF_3SO_3)_2$  hydrogel electrolyte. The CV curve at a sweep rate of  $1.00\text{ mV s}^{-1}$  shows a pair of redox peaks and large enclosed area (Figure 6b). As shown in Figure 6(c), the specific capacities of the battery are  $256.20$ ,  $187.00$ ,  $135.30$ ,  $100.10$ ,  $76.20$ , and  $30.10\text{ mAh g}^{-1}$  at  $1.00$ ,  $2.00$ ,  $3.00$ ,  $4.00$ ,  $5.00$ , and  $10.00\text{ Ag}^{-1}$ , respectively. Fortunately, a bit specific capacity of the battery is still reserved at such a high current density of  $10.00\text{ Ag}^{-1}$ . Besides, the battery also shows good rate capacities of  $252.4\text{ mAh g}^{-1}$  at  $1.00\text{ Ag}^{-1}$  and  $39.3\text{ mAh g}^{-1}$  at  $10.00\text{ Ag}^{-1}$  (Figure S13). Moreover, the battery retained  $60.10\%$  of its initial capacity after 1000 charge-discharge cycles at a large current density of  $10.00\text{ Ag}^{-1}$  (Figure 6d). GCD curves at a current density of  $2.00\text{ Ag}^{-1}$  under different bending states, together with the flexibility of the battery were displayed in Figures 6(e) and S14, respectively. The charging platforms have only a slight

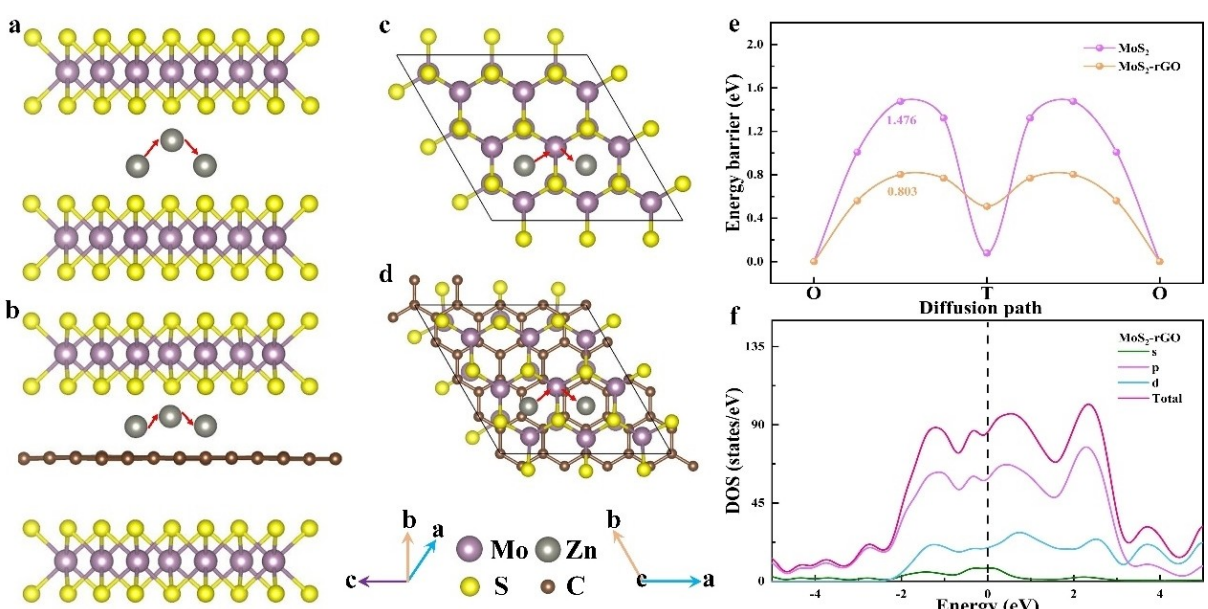


**Figure 5.** Theoretical calculation. a-d) Zn-ion diffusion paths in pristine  $MoS_2$  and  $MoS_2$ -rGO from a, b) the side view and c, d) top view. e) Migration energy barriers of pristine  $MoS_2$  and  $MoS_2$ -rGO. f) DOS of  $MoS_2$ -rGO.

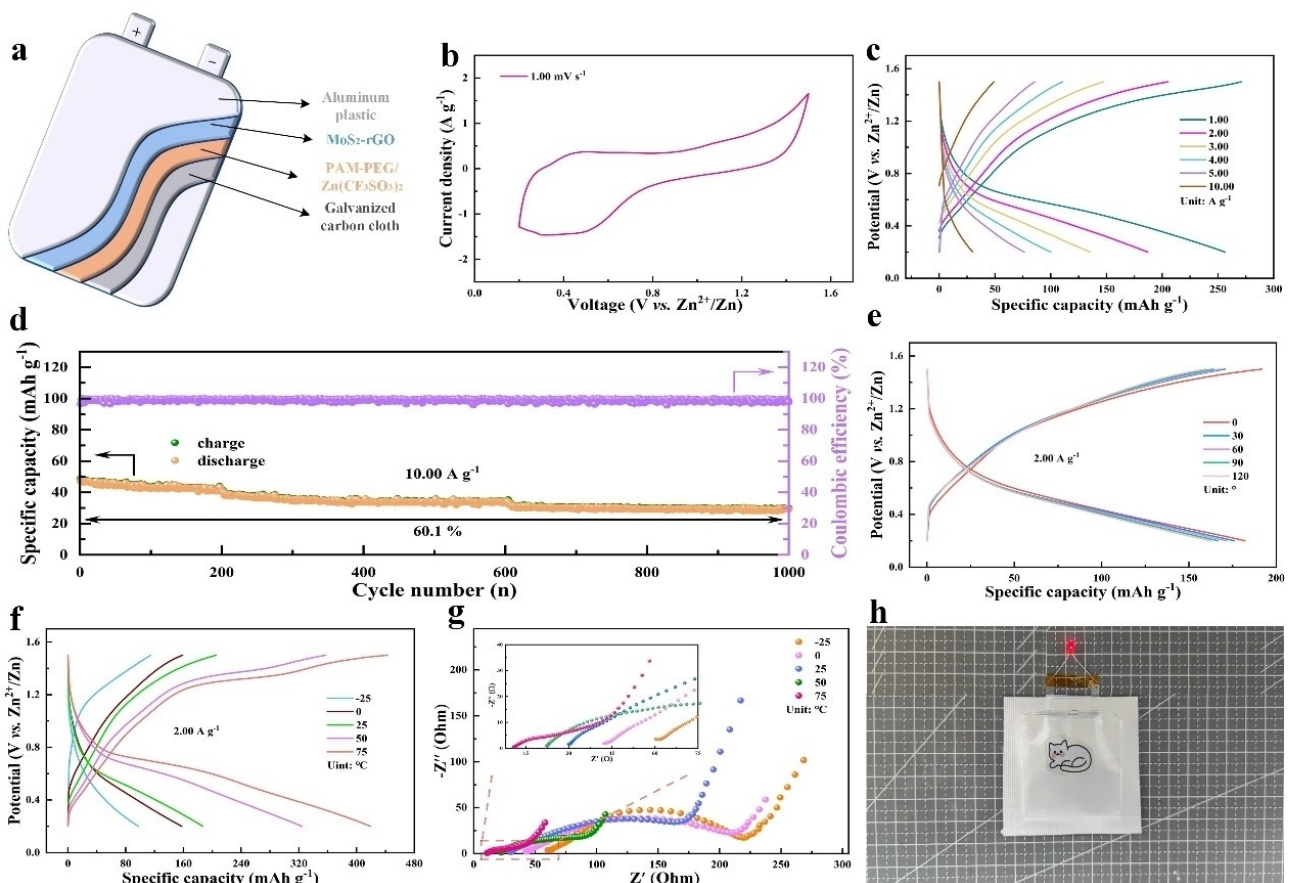


**Figure 6.** Electrochemical performances of the quasi-solid-state  $\text{MoS}_2\text{-rGO}/\text{Zn}$  battery. a) Schematic diagram. b) CV curve at  $1.00 \text{ mV s}^{-1}$ . c) GCD curves at various current densities from  $1.00$  to  $10.00 \text{ A g}^{-1}$ . d) Cycle life at  $10.00 \text{ A g}^{-1}$ . GCD curves at  $2.00 \text{ A g}^{-1}$  of e) different bending angles and f) different temperatures. g) EIS and magnified EIS (insert) plots at different temperatures. h) Photograph of the flexible  $\text{MoS}_2\text{-rGO}/\text{Zn}$  battery powering an LED.

increase and the discharge platforms are slightly decrease as bending angles increases, as a result, the fully discharged specific capacity at  $2.00 \text{ A g}^{-1}$  of the battery decreased by only  $16.80 \text{ mAh g}^{-1}$  from  $180.00 \text{ mAh g}^{-1}$  ( $0^\circ$ ) to  $163.20 \text{ mAh g}^{-1}$  ( $120^\circ$ ). Furthermore, the battery still retains  $90.60\%$  of the initial fully discharged specific capacity at  $2.00 \text{ A g}^{-1}$  after bending to  $120^\circ$  and the coulombic efficiency remains almost unchanged when the bending angles are extremely increased (Figure S15a). These results strongly prove that the battery can still supply energy stably under large flexible deformation. GCD curves at a current density of  $2.00 \text{ A g}^{-1}$  of the battery at different temperatures were presented in Figure 6(f). The discharged specific capacities of the battery are  $97.40$ ,  $156.70$ ,  $187.00$ ,  $314.20$ , and  $419.00 \text{ mAh g}^{-1}$  at  $-25^\circ\text{C}$ ,  $0^\circ\text{C}$ ,  $25^\circ\text{C}$ ,  $50^\circ\text{C}$ , and  $75^\circ\text{C}$ , respectively. As shown in Figure S15(b), the specific capacity of the battery gradually increases as the temperature rises whether charge or discharge. The increase in temperature will release more thermal energy, which strongly promotes the migration of  $\text{Zn}^{2+}$ , similarly, the coulombic efficiency increases gradually with the increasing temperature. The EIS curves at different temperatures from  $-25^\circ\text{C}$  to  $75^\circ\text{C}$  were measured to illustrate the effect of temperature on the battery (Figure 6g). All EIS curves contain a compressed

semicircle in the high-frequency region, the diameter of the semicircle represents the charge transfer resistance ( $R_{ct}$ ) and a sloped line in the low-frequency region. Obviously, the  $R_{ct}$  value decreased drastically with the gradual increase in temperature. As mentioned before, this result discloses that high temperature brilliantly spurs  $\text{Zn}^{2+}$  diffusion behavior and enhances the charge transfer kinetics. Impressively, the flexible soft-pack battery can be bent at different angles and successfully activated a light-emitting diode (LED) (Figure 6h), exhibiting great application prospects in the flexible electronic devices.

## Conclusion

In summary, a stable hierarchical heterostructure with seamless tight junction and unique conductive network is formed through in situ growing abundant 1T- $\text{MoS}_2$  nanoflowers on rGO nanosheets. The effective synergistic effect of a large amount of sulfur-deficient metallic 1T-phase  $\text{MoS}_2$  and rGO enables speedy and efficient transmission of electrons at the heterogeneous interface. Meanwhile, it also broadens the path for the diffusion of  $\text{Zn}^{2+}$  thanks to  $\text{MoS}_2$  nanoflowers grow firmly and disperse uniformly on rGO,

which effectively alleviates the stacking of MoS<sub>2</sub> and rGO layers. Consequently, the MoS<sub>2</sub>-rGO cathode in Zn(CF<sub>3</sub>SO<sub>3</sub>)<sub>2</sub> aqueous electrolyte achieved high discharge specific capacity (303.10 mAh g<sup>-1</sup> at 0.20 A g<sup>-1</sup>) and outstanding rate capability (102.70 mAh g<sup>-1</sup> at 20.00 A g<sup>-1</sup>, i.e., capacity retention of 33.88% for a 100-fold increase in current density). Electrochemical measurements and the systematic ex-situ investigations evidences the decent reaction kinetics of the MoS<sub>2</sub>-rGO cathode including desirable pseudocapacitive effects and the highly reversible insertion/extraction of Zn<sup>2+</sup>. DFT calculations illustrates that the MoS<sub>2</sub>-rGO cathode possesses the eminent conductivity and the low Zn<sup>2+</sup> diffusion barriers. Finally, the flexible quasi-solid-state MoS<sub>2</sub>-rGO//Zn battery employing the MoS<sub>2</sub>-rGO cathode and the PAM-PEG/Zn(CF<sub>3</sub>SO<sub>3</sub>)<sub>2</sub> hydrogel electrolyte indicates high electrochemical stability at different deformation states and different temperatures. This work presents more possibilities of applying layered materials as high-performance cathodes for AZIBs.

## Acknowledgements

F. L. and J. J. S. contributed equally to this work. This work is financially supported by the National Natural Science Foundation of China (No. 11674113 and 11874025) and Guangxi Distinguished Experts Special Fund (No. 2019B06). The authors would like to thank the technical support from the Analytical and Testing Center of HUST. Thank the Center of Optoelectronic Micro & Nano Fabrication and Characterizing Facility, Wuhan National Laboratory for Optoelectronics of HUST for the support in the SEM and TEM tests. Thank Nian Liu from Shiyanjia Lab ([www.shiyanjia.com](http://www.shiyanjia.com)) for the EPR and XPS analysis.

## Conflict of Interest

The authors declare no conflict of interest.

## Data Availability Statement

The data that support the findings of this study are available from the corresponding author upon reasonable request.

**Keywords:** flexibility · high and low temperature stability · MoS<sub>2</sub>-rGO heterostructure · ultra-quick Zn<sup>2+</sup> storage

- [1] Q. H. Zhao, A. Y. Song, S. X. Ding, R. Z. Qin, Y. H. Cui, S. N. Li, F. Pan, *Adv. Mater.* **2020**, *32*, 2002450.
- [2] J. H. Zhou, M. Xie, F. Wu, Y. Mei, Y. T. Hao, R. L. Huang, G. L. Wei, A. N. Liu, L. Li, R. J. Chen, *Adv. Mater.* **2021**, *33*, 2101649.
- [3] N. Zhang, X. Y. Chen, M. Yu, Z. Q. Niu, F. Y. Cheng, J. Chen, *Chem. Soc. Rev.* **2020**, *49*, 4203.
- [4] Y. X. Song, Y. Shi, J. Wan, B. Liu, L. J. Wan, R. Wen, *Adv. Energy Mater.* **2020**, *10*, 2000465.
- [5] X. F. Yang, K. R. Adair, X. J. Gao, X. L. Sun, *Energy Environ. Sci.* **2021**, *14*, 643.
- [6] Y. Fujii, D. Ramirez, N. C. Rosero-Navarro, D. Julian, A. Miura, F. Jaramillo, K. Tadanaga, *ACS Appl. Energ. Mater.* **2019**, *2*, 6569.
- [7] J. Liu, H. Yuan, H. Liu, C. Z. Zhao, Y. Lu, X. B. Cheng, J. Q. Huang, Q. Zhang, *Adv. Energy Mater.* **2022**, *12*, 2100748.
- [8] F. Liu, R. Xu, Y. C. Wu, D. T. Boyle, A. K. Yang, J. W. Xu, Y. Y. Zhu, Y. S. Ye, Z. A. Yu, Z. W. Zhang, X. Xiao, W. X. Huang, H. S. Wang, H. Chen, Y. Cui, *Nature* **2021**, *600*, 659.
- [9] Y. Lu, J. Chen, *Nat. Chem. Rev.* **2020**, *4*, 127.
- [10] Z. Y. Zhao, J. W. Han, F. Q. Chen, J. Xiao, Y. F. Zhao, Y. F. Zhang, D. B. Kong, Z. Weng, S. C. Wu, Q. H. Yang, *Adv. Energy Mater.* **2022**, *12*, 2103565.
- [11] R. F. Service, *Science* **2021**, *372*, 890.
- [12] Y. Y. Liu, X. Lu, F. L. Lai, T. X. Liu, P. R. Shearing, I. P. Parkin, G. J. He, D. J. L. Brett, *Joule* **2021**, *5*, 2845.
- [13] M. Fichtner, K. Edstrom, E. Ayerbe, M. Berecibar, A. Bhowmik, I. E. Castelli, S. Clark, R. Dominko, M. Erakca, A. A. Franco, A. Grimaud, B. Horstmann, A. Latz, H. Lorrman, M. Meeus, R. Narayan, F. Pammer, J. Ruhland, H. Stein, T. Vegge, M. Weil, *Adv. Energy Mater.* **2022**, *12*, 2102904.
- [14] H. Y. Liu, J. G. Wang, Z. Y. You, C. G. Wei, F. Y. Kang, B. Q. Wei, *Mater. Today* **2021**, *42*, 73.
- [15] Y. P. Deng, R. L. Liang, G. P. Jiang, Y. Jiang, A. P. Yu, Z. W. Chen, *ACS Energy Lett.* **2020**, *5*, 1665.
- [16] L. Ma, M. A. Schroeder, O. Borodin, T. P. Pollard, M. S. Ding, C. S. Wang, K. Xu, *Nat. Energy* **2020**, *5*, 743.
- [17] Y. B. Li, J. Fu, C. Zhong, T. P. Wu, Z. W. Chen, W. B. Hu, K. Amine, J. Lu, *Adv. Energy Mater.* **2019**, *9*, 1802605.
- [18] Y. H. Du, X. Y. Liu, X. Y. Wang, J. C. Sun, Q. Q. Lu, J. Z. Wang, A. Omar, D. Mikhailova, *Rare Met.* **2022**, *41*, 415.
- [19] W. C. Du, E. H. X. Ang, Y. Yang, Y. F. Zhang, M. H. Ye, C. C. Li, *Energy Environ. Sci.* **2020**, *13*, 3330.
- [20] J. Shin, D. S. Choi, H. J. Lee, Y. Jung, J. W. Choi, *Adv. Energy Mater.* **2019**, *9*, 1900083.
- [21] S. C. Liu, H. Zhu, B. H. Zhang, G. Li, H. K. Zhu, Y. Ren, H. B. Geng, Y. Yang, Q. Liu, C. C. Li, *Adv. Mater.* **2020**, *32*, 2001113.
- [22] Y. D. Jiao, L. Q. Kang, J. Berry-Gair, K. McColl, J. W. Li, H. B. Dong, H. Jiang, R. Wang, F. Cora, D. J. L. Brett, G. J. He, I. P. Parkin, *J. Mater. Chem. A* **2020**, *8*, 22075.
- [23] S. Islam, M. H. Alfaruqi, D. Y. Putro, S. Park, S. Kim, S. Lee, M. S. Ahmed, V. Mathew, Y. K. Sun, J. Y. Hwang, J. Kim, *Adv. Sci.* **2021**, *8*, 2002636.
- [24] N. Zhang, Y. Dong, M. Jia, X. Bian, Y. Y. Wang, M. D. Qiu, J. Z. Xu, Y. C. Liu, L. F. Jiao, F. Y. Cheng, *ACS Energy Lett.* **2018**, *3*, 1366.
- [25] C. Xia, J. Guo, Y. J. Lei, H. F. Liang, C. Zhao, H. N. Alshareef, *Adv. Mater.* **2018**, *30*, 1705580.
- [26] Z. G. Hou, X. Q. Zhang, X. N. Li, Y. C. Zhu, J. W. Liang, Y. T. Qian, *J. Mater. Chem. A* **2017**, *5*, 730.
- [27] W. J. Deng, Z. G. Li, Y. K. Ye, Z. Q. Zhou, Y. B. Li, M. Zhang, X. R. Yuan, J. Hu, W. G. Zhao, Z. Y. Huang, C. Li, H. B. Chen, J. X. Zheng, R. Li, *Adv. Energy Mater.* **2021**, *11*, 2003639.
- [28] Z. W. Sheng, P. C. Qi, Y. Lu, G. F. Liu, M. Y. Chen, X. L. Gan, Y. H. Qin, K. Y. Hao, Y. W. Tang, *ACS Appl. Mater. Interfaces* **2021**, *13*, 34495.
- [29] W. S. V. Lee, T. Xiong, X. P. Wang, J. M. Xue, *Small Methods* **2021**, *5*, 2000815.
- [30] P. Li, J. Y. Jeong, B. J. Jin, K. Zhang, J. H. Park, *Adv. Energy Mater.* **2018**, *8*, 1703300.
- [31] W. W. Xu, C. L. Sun, K. N. Zhao, X. Cheng, S. Rawal, Y. Xu, Y. Wang, *Energy Storage Mater.* **2019**, *16*, 527.
- [32] C. Chen, X. Q. Xie, B. Anasori, A. Sarycheva, T. Makaryan, M. Q. Zhao, P. Urbanowski, L. Miao, J. J. Jiang, Y. Gogotsi, *Angew. Chem. Int. Ed.* **2018**, *57*, 1846.
- [33] Y. L. Pan, L. L. Gong, X. D. Cheng, Y. Zhou, Y. B. Fu, J. Feng, H. Ahmed, H. P. Zhang, *ACS Nano* **2020**, *14*, 5917.
- [34] S. Pak, S. Jang, T. Kim, J. Lim, J. S. Hwang, Y. Cho, H. Chang, A. R. Jang, K. H. Park, J. Hong, S. Cha, *Adv. Mater.* **2021**, *33*, 2102091.
- [35] H. F. Li, Q. Yang, F. N. Mo, G. J. Liang, Z. X. Liu, Z. J. Tang, L. T. Ma, J. Liu, Z. C. Shi, C. Y. Zhi, *Energy Storage Mater.* **2019**, *19*, 94.
- [36] H. Y. Liu, J. G. Wang, W. Hua, Z. Y. You, Z. D. Hou, J. C. Yang, C. G. Wei, F. Y. Kang, *Energy Storage Mater.* **2021**, *35*, 731.
- [37] S. W. Li, Y. C. Liu, X. D. Zhao, K. X. Cui, Q. Y. Shen, P. Li, X. H. Qu, L. F. Jiao, *Angew. Chem. Int. Ed.* **2021**, *60*, 20286.
- [38] K. Qi, X. Q. Cui, L. Gu, S. S. Yu, X. F. Fan, M. C. Luo, S. Xu, N. B. Li, L. R. Zheng, Q. H. Zhang, J. Y. Ma, Y. Gong, F. Lv, K. Wang, H. H. Huang, W. Zhang, S. J. Guo, W. T. Zheng, P. Liu, *Nat. Commun.* **2019**, *10*, 5231.
- [39] K. Chang, X. Hai, H. Pang, H. B. Zhang, L. Shi, G. G. Liu, H. M. Liu, G. X. Zhao, M. Li, J. H. Ye, *Adv. Mater.* **2016**, *28*, 10033.

- [40] H. H. Huang, Y. Cui, Q. Li, C. C. Dun, W. Zhou, W. X. Huang, L. Chen, C. A. Hewitt, D. L. Carroll, *Nano Energy* **2016**, *26*, 172.
- [41] J. J. Wang, J. G. Wang, H. Y. Liu, Z. Y. You, Z. Li, F. Y. Kang, B. Q. Wei, *Adv. Funct. Mater.* **2021**, *31*, 2007397.
- [42] B. Wang, T. T. Ruan, Y. Chen, F. Jin, L. Peng, Y. Zhou, D. L. Wang, S. X. Dou, *Energy Storage Mater.* **2020**, *24*, 22.
- [43] J. W. Han, H. Li, Q. H. Yang, *Mater. Today* **2021**, *51*, 552.
- [44] Y. H. Dai, X. B. Liao, R. H. Yu, J. H. Li, J. T. Li, S. S. Tan, P. He, Q. Y. An, Q. L. Wei, L. N. Chen, X. F. Hong, K. N. Zhao, Y. Ren, J. S. Wu, Y. Zhao, L. Q. Mai, *Adv. Mater.* **2021**, *33*, 2100359.
- [45] X. Zhang, Y. Y. Liang, *Adv. Sci.* **2018**, *5*, 1700644.
- [46] J. R. He, G. Hartmann, M. Lee, G. S. Hwang, Y. F. Chen, A. Manthiram, *Energy Environ. Sci.* **2019**, *12*, 344.
- [47] Y. Q. Zhang, L. Tao, C. Xie, D. D. Wang, Y. Q. Zou, R. Chen, Y. Y. Wang, C. K. Jia, S. Y. Wang, *Adv. Mater.* **2020**, *32*, 1905923.
- [48] H. B. Lin, L. Q. Yang, X. Jiang, G. C. Li, T. R. Zhang, Q. F. Yao, G. W. Zheng, J. Y. Lee, *Energy Environ. Sci.* **2017**, *10*, 1476.
- [49] Y. Z. Song, W. L. Cai, L. Kong, J. S. Cai, Q. Zhang, J. Y. Sun, *Adv. Energy Mater.* **2020**, *10*, 1901075.
- [50] H. Y. Li, S. M. Chen, X. F. Jia, B. Xu, H. F. Lin, H. Z. Yang, L. Song, X. Wang, *Nat. Commun.* **2017**, *8*, 15377.
- [51] X. X. Han, X. L. Tong, X. C. Liu, A. Chen, X. D. Wen, N. J. Yang, X. Y. Guo, *ACS Catal.* **2018**, *8*, 1828.
- [52] V. Augustyn, P. Simon, B. Dunn, *Energy Environ. Sci.* **2014**, *7*, 1597.
- [53] W. Li, K. L. Wang, S. J. Cheng, K. Jiang, *Adv. Energy Mater.* **2019**, *9*, 1900993.

Manuscript received: March 8, 2022

Revised manuscript received: April 11, 2022

Accepted manuscript online: April 12, 2022

Version of record online: May 24, 2022